

---

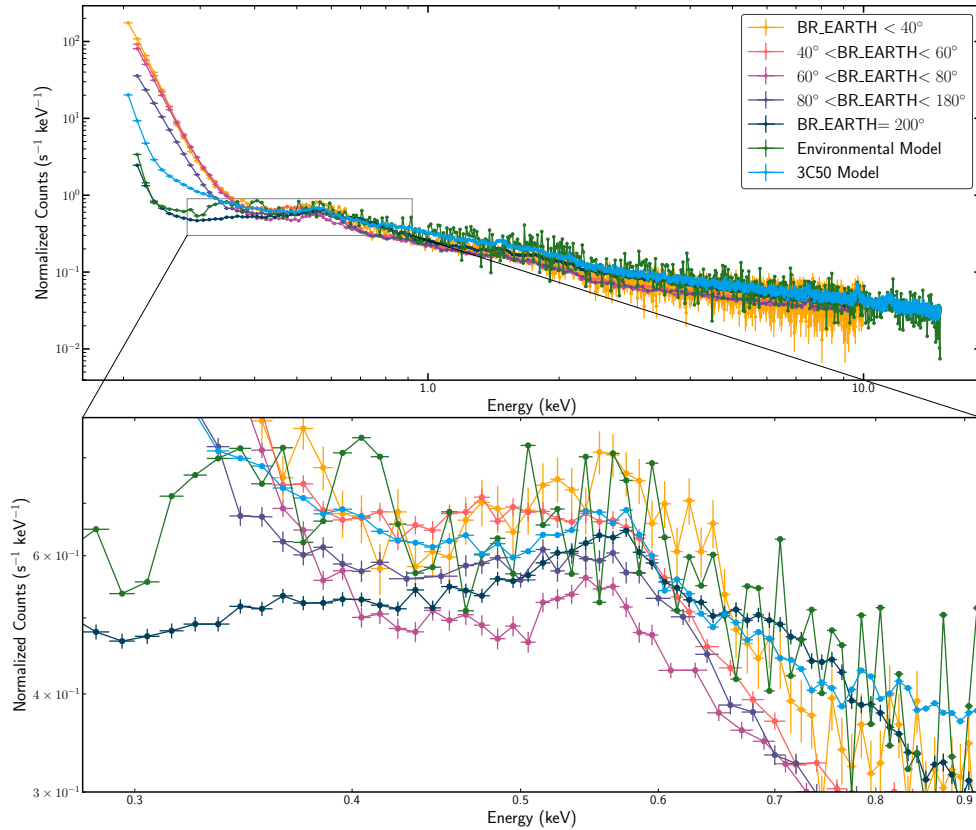
# A NICER VIEW OF THE X-RAY BACKGROUND

---

**Dominick Rowan**  
Haverford College  
Haverford, PA 19041  
dmrowan@haverford.edu

August 27, 2020

The soft X-ray background observed by *NICER* depends on the angular separation between the target and the illuminated Earth limb



## ABSTRACT

We present an investigation of the soft X-ray background observed by the Neutron Star Interior Composition Explorer (*NICER*). In any astronomical observation, the study of a source is only possible if the relevant background information is well characterized. Since *NICER* is a non-imaging telescope, we must use background estimation techniques that model the time-dependent background for our target observations. There are currently two background techniques in development specifically for *NICER* observations: the environmental model and the 3C50 model. We perform spectral analysis of blank sky observations taken over two years to investigate directions for future improvement of the background modeling methods. We identify the bright Earth angle – the angle between the *NICER* pointing and the bright Earth limb – as a relevant parameter for the intensity of the soft X-ray background. Finally, a comparison between the effects of bright Earth angle and Sun angle shows that both parameters should be included for accurate background estimation.

## 1 The Importance of X-ray Observations

Since the first detection of cosmic X-rays from Scorpius X-1 by [Giacconi et al. \(1962\)](#), X-ray astronomy has evolved from a niche field to an essential technique for the study of high-energy phenomena. When we observe sources like the Crab Nebula in the radio band, we can learn about the morphology of the supernova, including the ‘wisp’ structures at the edges ([Dubner et al., 2017](#)). Infrared observations distinguish between regions of hot and cold gas in the cloud ([Temim et al., 2006; Gomez et al., 2012](#)), while optical observations reveal filament-like structures spatially separated from those in the radio. At high energies, *Chandra* X-ray images show a young pulsar wind nebula at the center of the supernovae that is almost entirely invisible in the other bands. Each wavelength regime is effective for different types of astronomical objects. X-ray observations are most useful for studying high-energy phenomena where matter is accelerated to immense speeds. Three of the most targeted objects for X-ray observations are compact X-ray binaries, active galactic nuclei (AGN), and pulsars, where matter is accelerated by accretion processes and magnetic fields.

When the first cosmic X-ray source was detected [Giacconi et al. \(1962\)](#) the nature of the source was unclear. We now know that Sco-X1 is a compact binary formed of a neutron star and a low mass star. When black holes or neutron stars orbit with a companion star, accretion can drive matter from the companion star onto the compact object. The accretion can occur either through the inner Lagrangian Point, or from an extended source such as a wind nebula ([Lewin & van der Klis, 2010](#)). As particles interact with the disk, they dissipate energy and lose angular momentum, falling inwards and emitting high-energy radiation. X-ray observations of these sources enable study of accretion dynamics and dense matter properties (e.g., [Ray et al., 2019a](#)).

A similar accretion phenomena occurs at the center of galaxies, where we find high energy emission from the black hole accretion disk. We often observe galaxies with active galactic nuclei (AGN) as being highly variable with jets of emission ([Blandford et al., 2019](#)). AGN, similar to compact binaries, convert gravitational energy from infalling

material into electromagnetic radiation. The X-ray emission is expected to be produced through inverse Compton interactions between optical photons and a hot electron corona (Haardt & Maraschi, 1991). We also observe reflection features when X-rays pass through the broad line region and the molecular torus. Studying the X-ray emission of AGN therefore helps us study the dynamics of the central engine and the accretion disk.

High-energy emission also occurs when charged particles are accelerated in regions of dense magnetic fields. Many neutron stars develop high rotation rates and compact magnetospheres during formation. Since we observe regular pulses of emission in radio observations of these neutron stars, they are known as pulsars. At higher energies, we observe X-ray pulsar emission as charged particles are accelerated through the magnetosphere. While a number of emission models have been developed since the initial discovery of pulsars (e.g., Arons, 1983; Muslimov & Harding, 2003; Dyks & Rudak, 2003; Cheng et al., 1986; Verbunt et al., 1996), modern studies have shifted focus to the current sheet as the source of X-ray emission (Kalapotharakos et al., 2014; Cerutti et al., 2016). High-energy observations of millisecond pulsars offers a method by which to compare and adjust theoretical models.

## 1.1 X-ray Observatories

To make X-ray observations, we must take our instruments above the Earth's atmosphere, which is opaque to X-rays. Unlike optical or radio observations, which utilize ground based telescopes, early X-ray astronomy efforts used sounding rockets (Fraser, 1989) and high-altitude balloons (Bleeker et al., 1967). Poor angular resolution limited these observations. In fact, the highest precision X-ray observation in the 1960s was made of the Crab Nebula using the lunar occultation to identify the X-ray source (Bowyer et al., 1964). While detector technology continued to improve in the coming decades, with advancements such as back illuminated CCDs for low energy response and silicon drift detectors for timing accuracy, these systems were not fully taken advantage of until the advent of the satellite era.

Modern X-ray telescopes make continuous observations from outside Earth's atmosphere, either in Earth orbit or on the International Space Station. Uhuru, launched in 1970, was the first dedicated X-ray satellite (Murdin, 2000). The Uhuru satellite used two proportional counters to observe X-rays between 0.2–20.0 keV.<sup>1,2</sup> Uhuru made over 300 detections of X-ray sources, including binary stars, supernovae remnants, and galaxy clusters (Forman et al., 1978).

Since then, numerous X-ray telescopes have contributed the field with improved detector systems designed for different mission goals. In general, X-ray telescopes can operate in two modes: imaging and spectroscopy. An X-ray image of a source, such as the Crab Nebula from *Chandra* (Dubner et al., 2017), can be used to study spatial variations or symmetries in the object. Spectroscopic observations show the energy distribution of the detected photons. This allows for comparisons with theoretical models using tools like XSPEC (Arnaud, 1996). Figure 1 shows the years of operation for a number of X-ray telescopes. Here, we focus discussion on two of the most productive X-ray telescopes in recent history before describing the Neutron Star Interior Composition Explorer (*NICER*).

---

<sup>1</sup>[https://heasarc.gsfc.nasa.gov/docs/uhuru/uhuru\\_about.html](https://heasarc.gsfc.nasa.gov/docs/uhuru/uhuru_about.html)

<sup>2</sup>X-ray observations are typically described in units of energy. If we were to use frequency, like radio observations, or wavelength, as we do in optical, the numbers quickly become unwieldy. Typical X-ray wavelengths correspond to  $\sim 1.2$  nm or  $2.5 \times 10^{17}$  Hz, both of which are more inconvenient than 1 keV.

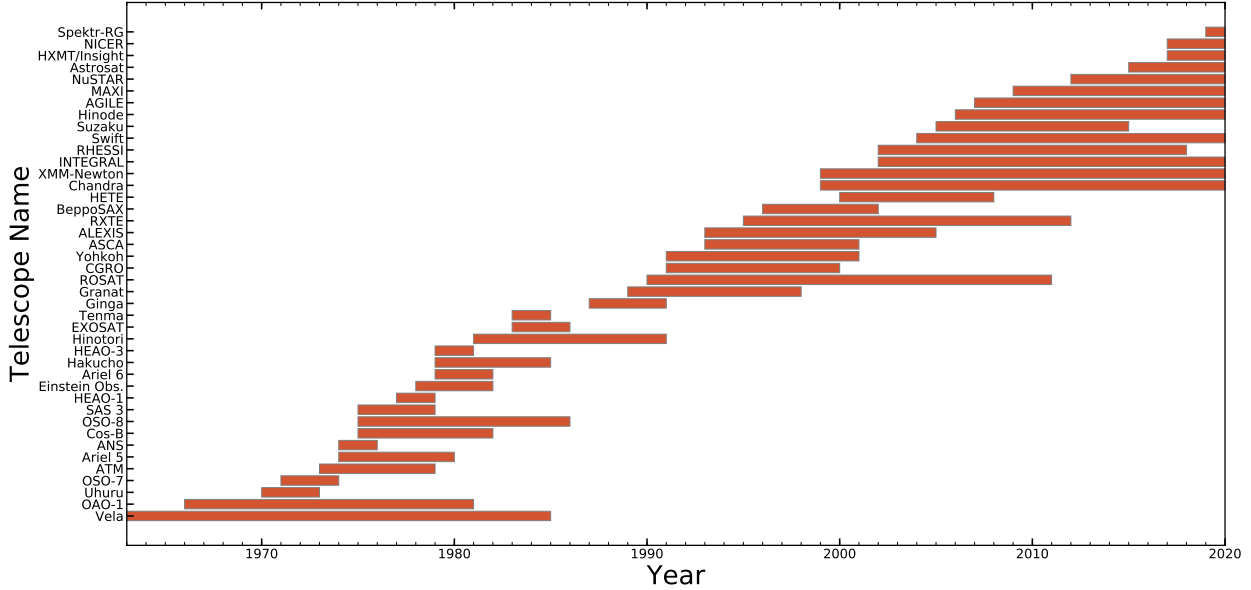


Figure 1: Notable X-ray observatories organized by mission dates ([Wikipedia contributors, 2020](#)). Here, we focus discussion on *XMM-Newton* and *Chandra*, two of the most productive and long-lasting X-ray observatories, and *NICER*, launched in 2017.

*XMM-Newton* ([Jansen et al., 2001](#)), launched in 1999, carries three European Photon Imaging Cameras (EPIC): two metal oxide semiconductor (MOS) CCDs ([Turner et al., 2001](#)), and one p-n junction multilinear CCD ([Strüder et al., 2001](#)). Two reflection grating spectrometers also lie in the focal plane of the X-ray telescope for high resolution spectroscopy of soft X-rays. Both types of instruments are capable of measuring the energy of detected photons. There is also an onboard EPIC Radiation Monitor (ERM) that measures particle information, detects radiative belts, and monitors Solar flares. The three *XMM-Newton* telescopes each have 58 Wolter I mirrors, which are cylindrically nested to increase the number of reflected photons. While *XMM-Newton* was originally scheduled as a two year mission, it continues to produce novel results even after 20 years of operation. The observatory has contributed to the field of X-ray astronomy with high energy pulsar measurements (e.g., [Ng et al., 2014](#)), AGN observations and the first black hole spin measurement ([Risaliti et al., 2013](#)). The large effective area of  $\sim 1500 \text{ cm}^2$  at 1.0 keV ([Lumb et al., 2012](#)) has also enabled spectra analysis of the cosmic X-ray background ([Lumb et al., 2002](#)).

A discussion of X-ray telescopes can not be complete without mentioning *Chandra*, launched in 1999 ([Weisskopf et al., 2000](#)). *Chandra* observes between 0.08–10.0 keV on a highly elliptical Earth orbit with a period of 63.5 hours, allowing up to 55 hours of continuous observation. Like *XMM-Newton*, *Chandra* uses nested paraboloid-shaped mirrors to focus incoming X-ray photons. Since the telescope only uses four nested mirrors, with diameters ranging from 65 to 123 cm, *Chandra* sacrifices effective area for improved sensitivity.

The *Chandra* detector system is also made up of multiple gratings and CCD systems. The low energy transmission grating makes spectroscopic measurements between 0.08–2.0 keV, while the high energy transmission grating uses two facets, one operating from 0.4–4.0 keV and the other from 0.8–8.0 keV. The Advanced CCD Imaging Spectrometer

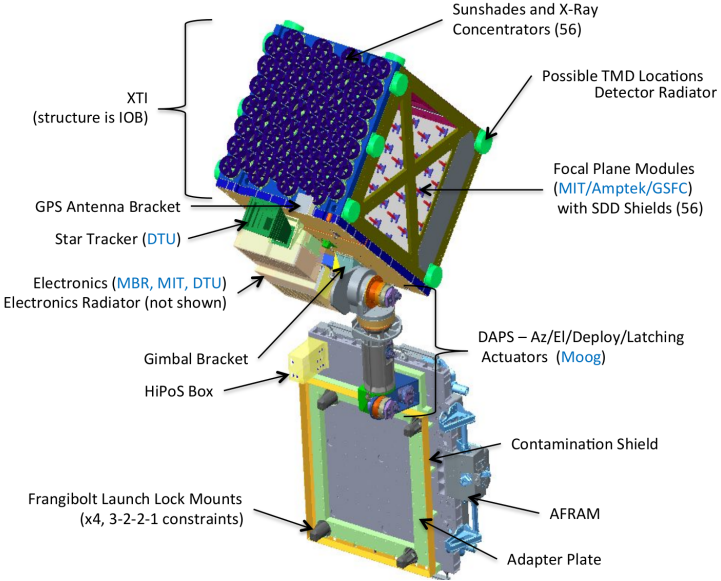


Figure 2: Diagram of the *NICER* instrument from [Okajima et al. \(2016\)](#).

(ACIS) is made up of two array components. The ACIS-I has four CCDs in a square configuration for high resolution imaging, while the ACIS-S uses 6 CCDs in a linear configuration for high resolution spectroscopy. *Chandra* has provided high resolution images of supernovae (e.g., [Hwang & Laming, 2012](#)), observations of black hole accretion (e.g., [Miller et al., 2017](#)), and constraints on dark energy (e.g., [Allen et al., 2008](#)).

## 1.2 The Neutron Star Interior Composition Explorer

Unlike *Chandra* or *XMM-Newton*, which are independent satellites, the *NICER* was deployed on the International Space Station (ISS) in June of 2017 ([Gendreau & Arzoumanian, 2017](#)). *NICER* observes X-ray photons from 0.2 – 12.0 keV with a large effective area of  $1900 \text{ cm}^2$  at 1.5 keV. The X-ray telescope instrument (XTI) is made up of 56 X-ray concentrators ([Okajima et al., 2016](#)) paired with 56 focal plane modules (FPMs, [Prigozhin et al., 2016](#)). Figure 2 shows a schematic of the instrument from [Okajima et al. \(2016\)](#). Each focal plane module contains a silicon drift detector (SDD). Unlike other X-ray telescopes, the SDDs are deliberately kept small with areas of  $25 \text{ mm}^2$  to minimize delays from electron drift times between the photon interaction sites and detector anode. While this prevents X-ray imaging, *NICER* boasts absolute timing accuracy  $< 300 \text{ ns}$ . By combining high precision timing and energy measurements, *NICER* can perform spectral and temporal analysis simultaneously.

As the instrument name suggests, the primary mission goal for this telescope is to probe the composition of neutron stars. Since these stars are some of the densest objects in the universe, second only to black holes, they offer a unique lens into high density nuclear physics. Theoretical studies of core composition have suggested a number of exotic states, including hyperons ([Glendenning, 1985](#)) and strange quark matter ([Lattimer & Prakash, 2007](#)). While a number of theoretical models for the neutron star equation of state exist, observational evidence is needed to identify the true solution. Fortunately, the equation of state can be described in terms of stellar mass and radius. Neutron star

masses have been calculated through measurement of binary orbits, taking relativistic effects into account (Thorsett & Chakrabarty, 1999; Nice, 2006). Radius measurements have proven more difficult. By modeling the thermal emission regions for X-ray pulsars, Riley et al. (2019) and Miller et al. (2019b) have recently used *NICER* observations to find simultaneous mass and radius measurements for PSR J0030+0451. Ongoing work is being done to perform the same analysis for additional thermal X-ray pulsars and to provide theoretical interpretations of the results (Raaijmakers et al., 2019; Bilous et al., 2019).

While the observation of neutron stars for the purpose of mass and radius measurements is the primary goal, *NICER* has contributed to a number of subfields of X-ray astronomy. *NICER* observations of neutron stars have also enabled study of thermonuclear X-ray bursts (e.g., Arzoumanian et al., 2019), timing measurements for pulsar timing arrays (Deneva et al., 2019), and discovery of X-ray pulsations (e.g., Ray et al., 2019b). Measurements of reflection spectroscopy and reverberation studies from black hole X-ray binaries have described accretion disk geometries (e.g., Wang et al., 2019). Similar reflection spectroscopy measurements around low mass X-ray binaries have found spectral features that can be used to describe the accretion disk (Ludlam et al., 2018). *NICER* has also played a key role in X-ray observations of transient sources (e.g., Kara et al., 2019).

### 1.3 Background Modeling in *NICER* Observations

*NICER* has already produced numerous novel results, and there is even more room for expanding the scientific impact. Some of the observational challenges faced by *NICER* are similar to those encountered by other X-ray telescopes early in their missions. The *NICER* instrument response, effective area, and gain calibration has gone through numerous iterations since first light, improving the accuracy of spectral parameters. While some telescopes, such as *XMM-Newton*, have used a Bayesian framework to incorporate instrumental calibration uncertainties into spectral observations (Lee et al., 2011), no such technique currently exists for *NICER*. In order to disentangle astrophysical features from instrument response artifacts, multi-telescope observations can be used to cross-check detections, improving detection statistics simultaneously (e.g., Ludlam et al., 2018).

Even when observing the brightest targets, X-ray telescopes only measure a handful of X-ray photons each second. It is therefore crucial to have a fine-tuned reduction procedure to get from raw observations to science data without throwing out ‘good’ photons. As with any observation in any wavelength of light, our observations contain photons from the source and from the background. For the faintest X-ray sources, the background may contribute up to 90% of the observed X-ray counts. The X-ray background can be broadly divided into three components: a cosmic X-ray background from distant sources (Giacconi et al., 2001), a Galactic foreground component (Snowden et al., 1995; Kuntz & Snowden, 2000), and a particle induced background (Kuntz & Snowden, 2008; Bartalucci et al., 2014).

Some telescopes, such as *XMM-Newton*, use the wide FOV to capture source and background images on the same chip (Ng et al., 2014). *BeppoSAX* (Boella et al., 1997) takes an alternate, approach, continuously rocking the collimators on and off source to measure the background at the expense of target exposure time. To measure the particle background,

both *XMM-Newton* and *Chandra* include radiation monitors that can inform background modelling. Since the area of the *NICER* SDDs is small, there is no off-source region of the chip to use as an estimate of the background. Therefore, the mission-specific *NICER* background estimation techniques rely on a library of blank sky observations. Since we expect the background to depend on pointing and observation time, a standard time-independent background model is insufficient for *NICER* spectra analysis. By combining the blank sky observations with relevant parameters of a target observation, the *NICER* background estimation tools compute a scaled background corresponding to the time of a target observation. There are currently two independent background modeling techniques in development for *NICER* observations. The detector statistics model, more commonly known as the 3C50 model, considers internal metrics measured by the instrument. The environmental model, also referred to as the spaceweather model, uses external parameters of the observation to describe the time dependent background.<sup>3</sup>

These background models allow for detailed spectra analysis of *NICER* X-ray observations. The environmental model has been used in analysis of active galactic nuclei (Miller et al., 2019a), ultra-luminous X-ray pulsars (Ray et al., 2019a), transient magnetars (Güver et al., 2019), and pulsar searches (Ray et al., 2019b). The 3C50 model has been used in a study of reverberation and reflection in an X-ray black hole binary (Wang et al., 2019) and a study of a long period pulsar (Morello et al., 2019).

However, these background estimation models are far from complete. In soft X-ray observations of millisecond pulsars, two studies (Ray et al., 2019b; Rowan et al., 2020) have identified inaccuracies in the environmental model at soft X-rays. Figure 3 shows emission spectra from PSRs J0218+4232 and J1231-1411. In order to perform spectral analysis, additional Gaussian components corresponding to the background-modeling residuals had to be included. These soft X-ray features are consistent with energies from exospheric and Solar wind constituents.

#### 1.4 X-ray Background from the Solar Wind

The Solar wind originates in coronal holes on the surface of the Sun, and is composed of 92% hydrogen, 8% of helium, and  $\sim 1\%$  heavy elements (Cravens et al., 2009). When these heavier elements collide with an ionized medium, such as the geocorona, charge transfer collisions result in excited product ions. Cravens et al. (2009) gives an example reaction:



where M is a neutral target. The X-ray emission from de-excitation (of  $\text{O}^{6+*}$ , in this case) falls in the soft X-ray regime. The O VII multiplet has emission lines at 560.9, 568.5 and 574 eV. The O VIII Lyman alpha line is at 653.1 eV (Koutroumpa et al., 2009). At softer energies, there are C VI lines at 370 and 460 eV. Near 250 eV, there are also lines from Fe, Si, S, and Mg. These emission features are consistent with the energies underestimated with background models shown in Figure 3.

---

<sup>3</sup>Mission documentation for these models can be found [here](#).

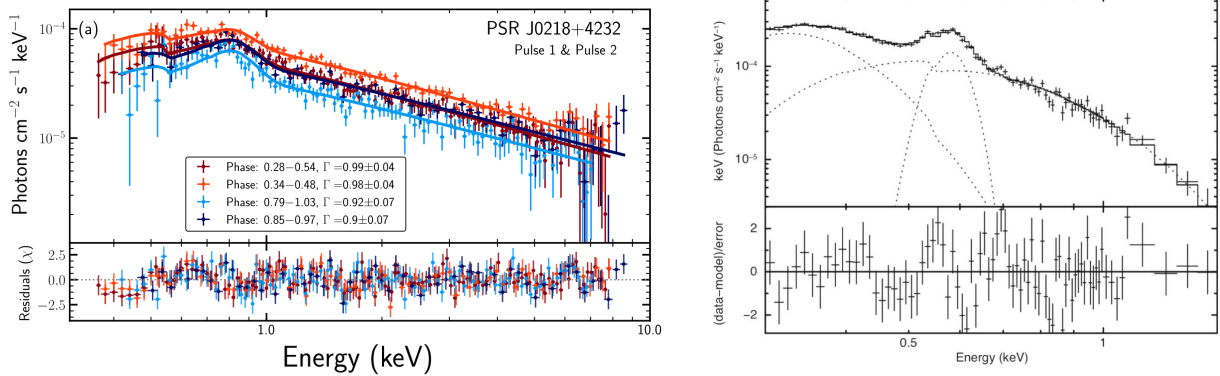


Figure 3: Left: Phase-resolved *NICER* emission spectra of millisecond pulsar PSR J0218+4232 from Rowan et al. (2020) showing soft X-ray residuals at  $< 1$  keV. Right: similar feature observed in emission spectra of PSR J1231-1411 Ray et al. (2019b). Including the bright Earth angle as an additional parameter in the environmental model may remove the need for fitting a Gaussian emission feature.

The effects of Solar wind have been observed by other X-ray telescopes, most notably *XMM-Newton* and *Suzaku* (Snowden et al., 2004; Carter & Sembay, 2009; Fujimoto et al., 2007). The magnitude of these effects depends on the specific observing geometry and on temporal variation in the Solar wind (Snowden et al., 1995). In this work we seek to identify additional observational parameters that are correlated to the soft X-ray *NICER* X-ray background. Although the environmental model currently considers the Sun angle parameter, it does not take into account the angle between *NICER* and the illuminated Earth limb. Figure 4 shows a schematic of the bright Earth angle. When *NICER* is pointing closer to the illuminated Earth limb, we expect to find excess soft X-ray emission. This would make the bright Earth angle a useful metric for background estimation routines.

In this work we measure spectral variations of blank sky observations as a function of bright Earth angle. In doing so, we identify directions for improving the *NICER* background estimation techniques. We describe the *NICER* observations in Section §2. We discuss our spectra extraction procedure in §3 and present bright Earth angle dependencies. Section §4 describes the two background models currently in use and how they compare to our blank sky observations. We then perform an additional analysis on the effects of Sun angle in Section §5 before discussing our results and offering directions for improvement in Section §6.

## 2 *NICER* Observations

To characterize the *NICER* X-ray background we observe patches of the sky with no X-ray sources. *NICER* has been regularly observing seven such regions since 2017 that were originally used for *RXTE* instrument calibration (Jahoda et al., 2006). We plot the seven regions in ICRS coordinates in Figure 5.

We use a total number of 955 observations across the seven regions. Table 1 gives the total number of observations and exposure for each background region. For each observation we run the HEASoft 6.26 task `nicerl2`.<sup>4</sup> This applies

<sup>4</sup><https://heasarc.gsfc.nasa.gov/lheasoft/ftools/headas/nicerl2.html>

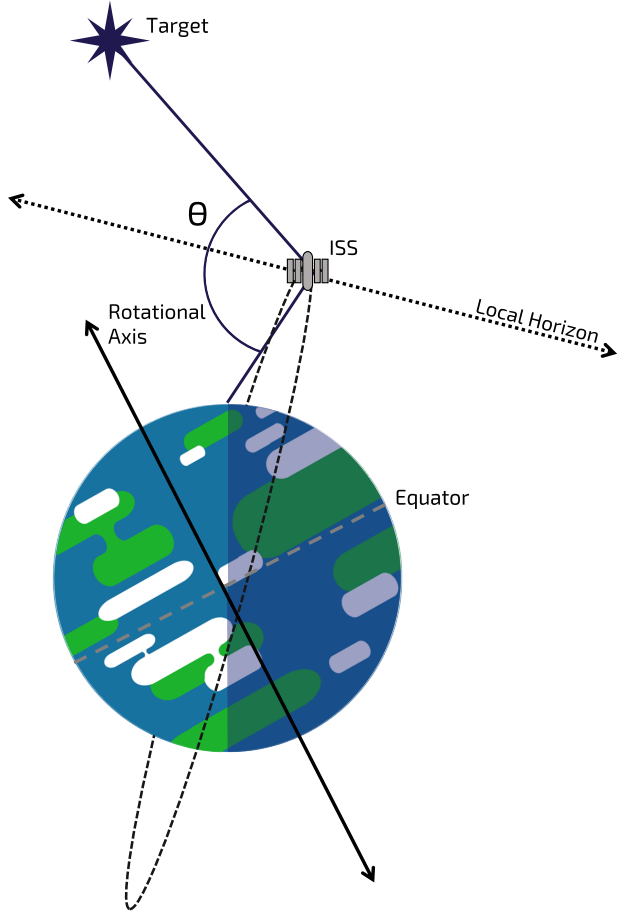


Figure 4: The bright Earth angle is defined as the angle between the source and the bright Earth limb, given as  $\theta$  in this diagram. For observations taken over the dark Earth limb, the bright Earth angle is set to the default HEAsoft value of  $200^\circ$ .

Table 1: We use observations from 7 background regions originally designated for RXTE. In total, we have 955 observations.

Region	Number of ObsIDs	Total Exposure (ks)	Right Ascension	Declination
BKGD_RXTE_1	163	2680	$5^\circ$	$-67^\circ$
2	141	4365	$60^\circ$	$2^\circ$
3	174	2601	$138^\circ$	$15^\circ$
4	95	3904	$30^\circ$	$10^\circ$
5	132	4518	$-15^\circ$	$-18^\circ$
6	134	6369	$160^\circ$	$72.57^\circ$
8	116	4266	$-176.3^\circ$	$53.3^\circ$
Total:	955	28703		

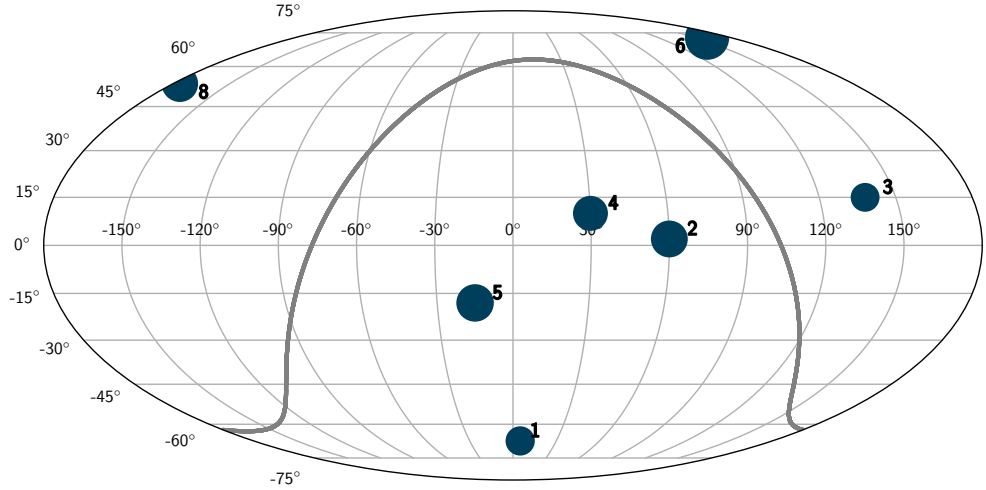


Figure 5: Equatorial sky projection with the seven background regions marked with the original RXTE ID numbers. The size of the marker is scaled to represent the amount of exposure on each region (Table 1). The plane of the Milky Way is overplotted in gray.

the standard processing steps including calibrating fast and slow channels, making timing corrections, and applying initial screening criteria. This is sometimes referred to as level 2 processing since it considers additional observation parameters and diagnostics beyond those used in the original task.<sup>5</sup>

Each observation directory contains a filter file (with extension mkf).<sup>6</sup> The filter file contains over 90 columns for observational parameters as a function of time, including coordinate information, FPM statistics, and Soyuz rocket states. We use the *NICER*soft routine `add_kp` to include Potsdam geomagnetic planetary index ( $K_p$ ) values to the filter file of each observation. This parameter describes the magnitude of geomagnetic storms and is used in the environmental model. We then apply additional filtering to select photon events for analysis. Between `nicerl2` and our filtering, our cleaned events meet 14 criteria. Here we briefly describe each filtering expression.

We avoid passages above the South Atlantic Anomaly (SAA), a region where satellites experience high radiation levels. We use the *NICER*-specific SAA contour rather than the less restrictive contour defined in HEAsoft:

1. `nicersaafilt=YES`
2. `saafilt=NO`

---

<sup>5</sup>The `niprefilter2` help file explains the differences between level 1 and level 2 in greater detail.

<sup>6</sup>A breakdown of the *NICER* observation directory structure can be found in the [mission guide](#).

We ensure that pointing is within 0.015 degrees of the target, and check that both the instrument tracker and star tracker are functioning properly with

3. `trackfilt=YES`
4. `angular distance < 0.015°`
5. `st_valid=YES`

The elevation angle (ELV) describes the altitude of the target relative to the Earth limb. We set the minimum Earth elevation angle to standard 20°, but allow all bright Earth angles (BR\_EARTH) for the purposes of this analysis:

6. `ELV > 20°`
7. `BR_EARTH > 0°`

We require that at least 38 of the 52 operational FPMs are in use during a given time:

8. `min_fpm = 38`

We set criteria to minimize times of high radiation background, known as overshoot rates, and times of high optical loading, known as undershoot rates. These filtering expressions were designed to help select times with minimal background ([Gendreau, 2019](#)):

9. `FPM_UNDERONLY_COUNT < 200`
10. `FPM_OVERONLY_COUNT < 1`
11. `FPM_OVERONLY_COUNT < 1.52 * COR_SAX-0.633`

We can also set restrictions based on space weather, using the cutoff rigidity `COR_SAX`, planetary geomagnetic index  $K_p$ , and Sun angle using the filtering expressions. We discuss the physical relevance of these parameters in more detail in Section §[4.2](#).

12. `COR_SAX > 1.914 * Kp0.684 + 0.25`
13.  $K_p < 5$
14. `SUN_ANGLE > 60°` or `SUNSHINE=0`

We use the task `nimaketime` to generate good time intervals (GTIs) corresponding to these filter expressions. We extract events from these GTIs for each MPU using `niextract-events` resulting a single event file (extension evt) for each observation. We apply the same criteria to the filter file using `ftcopy`. Since none of these regions contain any X-ray sources, we consider them as a single set of background observations for the purposes of our analysis. We use `niextract-events` again to merge the event files of each observation, and `ftmerge` to merge the filter files. The result of our pipeline procedure is one event file and one filter file that we can use to assess the spectral dependence on bright Earth angle.

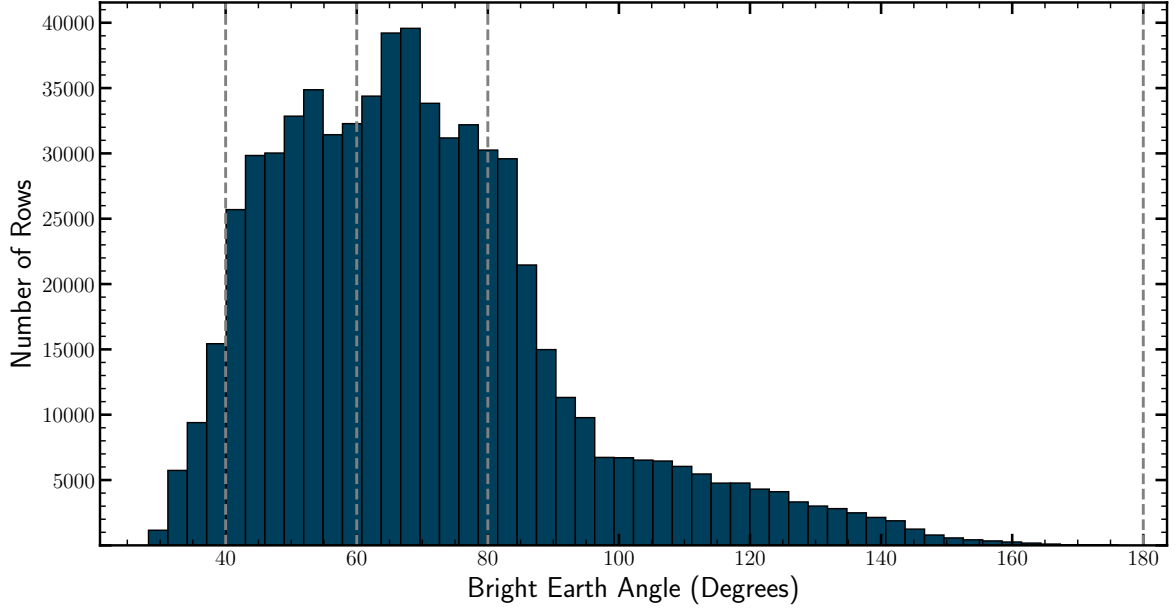


Figure 6: Histogram of bright Earth angles in the filter file (key BR\_EARTH). Each row of the filter file corresponds to one second of observation. When observations are taken over the dark Earth, the bright Earth angle is set to 200°. These values are not pictured on the histogram. The vertical lines indicate the boundary for the five bright Earth regions we choose for spectra extraction.

### 3 Spectra Extraction

Before extracting spectra corresponding to different bright Earth angles, we first plot the distribution of bright Earth angles for our observations. Figure 6 shows the distribution of bright Earth angles for SUNSHINE= 1. If the observation is taken during the night, the sunshine flag is zero and the bright Earth angle is set to 200°. This is the case for about  $\sim 40\%$  of observations.

We choose 5 ranges of bright Earth angle to extract spectra over:  $\text{BR\_EARTH} < 40$ ,  $40^\circ < \text{BR\_EARTH} < 60^\circ$ ,  $60^\circ < \text{BR\_EARTH} < 80^\circ$ ,  $80^\circ < \text{BR\_EARTH} < 180^\circ$ , and  $\text{BR\_EARTH} = 200^\circ$ . For each of these ranges we repeat the procedure of `nimaketime`, `niextract-events`, and `ftcopy` to generate separate GTIs, event files, and filter files. To extract a spectrum we follow the procedure of [Rowan et al. \(2020\)](#), which we summarize here. We first extract the spectrum from an event file with XSELECT v.2.4. Since we've performed bright Earth angle filtering directly with HEAsoft, we do not do any additional filtering in XSELECT. We use the `extract` command to bin our event file and generate a pha spectrum file. The spectrum file gives the number of X-ray counts per channel.

When we observe an X-ray source, the recorded data is the number of photons detected in each instrument channel  $n$  ([Arnaud et al., 1999](#)). This is related to the intrinsic spectrum of the source,  $f(E)$ , where  $E$  is energy, and the response function of the instrument,  $R(n, E)$ , by

$$C(n) = \int_0^{\infty} f(E)R(n, E)dE \quad (2)$$

In reality, we don't have a continuous function for  $R(n, E)$  but rather a matrix that defines a discrete function defined as

$$R_D(n, m) = \frac{\int_{E_{m-1}}^{E_m} R(n, E) dE}{E_m - E_{m-1}} \quad (3)$$

where  $m$  is the index of the energy range. We use XSPEC v.12.10.1 (Arnaud, 1996) to apply the instrument redistribution matrix file an auxiliary response file (version 1.02), transforming the channel axis to energy (keV). Since the exposure differs between the bright Earth spectra, we use normalized counts  $\text{s}^{-1} \text{ keV}^{-1}$  as the axis for comparison.

Figure 7 shows the five background spectra extracted over different ranges of bright Earth angle. We find clear evidence for bright Earth angle dependence, especially at the lowest energies. This immediately supports the relevance of the bright Earth angle for background estimation.

A closer look at the 0.3 – 0.9 keV regime (bottom panel of Figure 7) yields a number of insights. We find that the  $\text{BR\_EARTH} < 40^\circ$  spectra is generally consistent with the  $40^\circ < \text{BR\_EARTH} < 60^\circ$ , although we note larger uncertainties in the former spectrum due to low counts. If the effects of the local particle environment scaled linearly with bright Earth angle, we might have expected to see the spectra ordered by angle on the y-axis. However, we find the fewest counts  $\text{s}^{-1} \text{ keV}^{-1}$  in the bright Earth angle  $60^\circ < \text{BR\_EARTH} < 80^\circ$  range. This, combined with the large discrepancies between the  $60^\circ < \text{BR\_EARTH} < 80^\circ$  and  $40^\circ < \text{BR\_EARTH} < 60^\circ$  range, suggests that the soft X-ray background has a more complex dependence on bright Earth angle.

We also note that at energies  $> 0.7 \text{ keV}$ , the dark Earth ( $\text{BR\_EARTH} = 200^\circ$ ) spectrum exceeds all illuminated Earth spectra except the lowest bright Earth angle range. A further investigation into the effects of elevation angle in dark Earth observations may be useful to explain this observation.

Having demonstrated some dependence on the soft X-ray background with viewing geometry, we now compare our observations with background models. We use the environmental model and the 3C50 detector statistics model to make additional comparisons and suggest potential areas for improvement.

## 4 Comparison with Background Models

### 4.1 Detector Statistics Background Model

The 3C50 model uses internal detector metrics and is based on observations of the seven blank fields. The model takes advantage of the two analog chains used to process each photon event. The "fast" chain records timing measurements and has a quick rise time (84 ns), while the "slow" chain with a slower peaking time (465 ns) produces more precise amplitude measurements. In practice, the timing accuracy of each varies minimally, but the ratio between the amplitudes,  $\text{PI/PI\_FAST=PI\_RATIO}$ , can be a useful tool for subtracting background events. We expect a source photon to have similar energy measured by both chains so that the ratio is  $\sim 1$ .

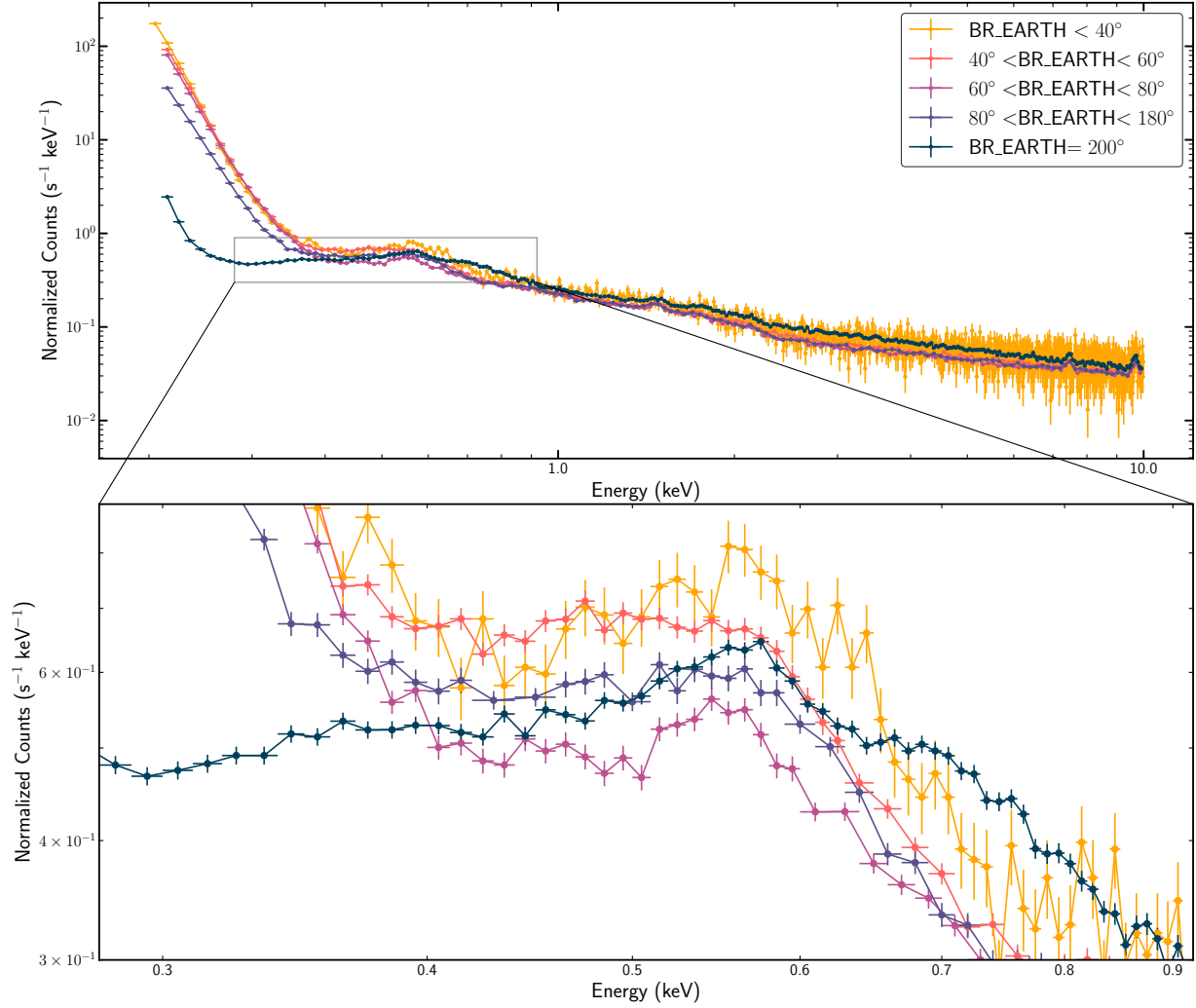


Figure 7: Comparison of spectra from background regions extracted over different bright Earth angle ranges. The bottom panel shows a zoom in on the 0.3 to 0.9 keV regime. We see evidence for stratification, especially at lower energies.

To understand the physical meaning of the energy ratio, it is necessary to describe the detector system in some detail. Unlike a charge coupled device (CCD), a silicon drift detector continuously reads out charges (Strüder, 2000). When a X-ray hits the surface of the SDD, the number of charge carriers created by the interaction is dependent on the energy of the X-ray (Rodney & Tonry, 2006). This charge cloud diffuses as it travels from the initial interaction point to the collection anode. If a particle has to travel longer on the SDD, it will have a larger cloud and require a longer collection time. This means that the fast chain will ‘clip’ the measurement and record a lower energy – the PI\_RATIO will be greater than 1. We expect all of our X-ray photons from the science target to be focused and therefore not spatially extended. In summary, the PI\_RATIO is useful for identifying detected events as being out-of-focus.

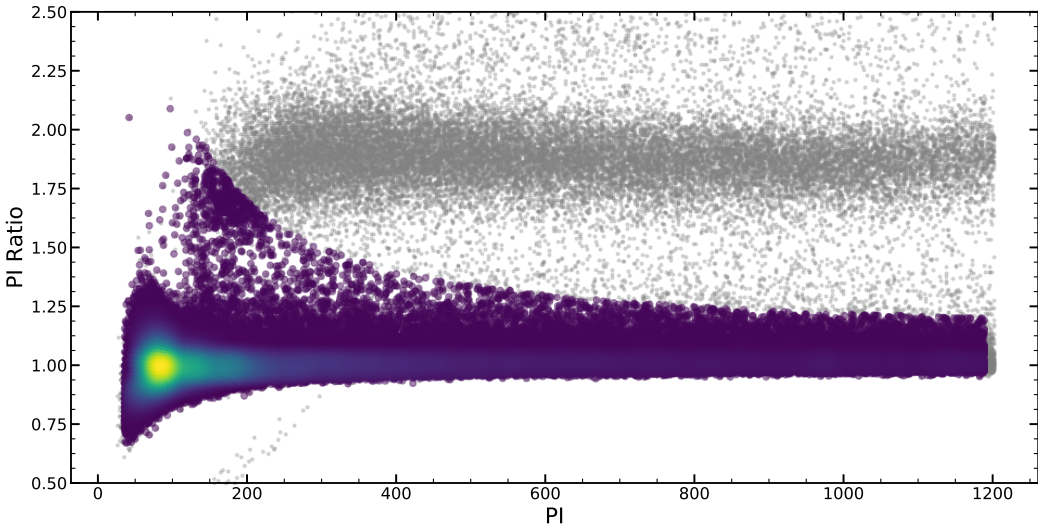


Figure 8: Example of a trumpet cut used for *NICER* observations of PSR B1821–24. In standard filtering, the gray events are filtered out as spatially extend detections. Non-rejected events are colored by density. For the 3C50 model, the distribution of photons detected in each component is used for normalization with a background library.

For a given observation, spatially extended photons are rejected in standard filtering procedures. Figure 8 shows an example of the cut made in the PI-PI\_RATIO space. We find a component near PI\_RATIO of 1, and a second population of events at higher ratios (shown in gray) that is not from the source. Since the cut takes the shape of a horn, this is known as a trumpet cut. The standard equation for the trumpet cut is

$$\text{PI\_RATIO} \equiv \text{PI}/\text{PI\_FAST} > 1.1 + 120/\text{PI}. \quad (4)$$

Figure 8 shows the events filtered out by the trumpet cut in gray. Although we remove these events in filtering, they serve as a useful diagnostic for the amount of unfocused background in a given observation.

The 3C50 model describes the count rate in three regions of the PI-PI\_RATIO space. The high-energy background (IBG)<sup>7</sup> region is for photons with energy between 15.0–18.0 keV that satisfy the criteria of Equation 4. The hatchet-rejected (HREJ) region is for photons with  $\text{PI\_RATIO} > 1.54$  and energy between 3–18 keV. The third region, NZ, considers the soft X-ray noise from particles with energies < 0.2 keV. The relative population of events in these regions will vary from between observations. Figure 9 (Remillard, 2019) shows two observations, one where the HREJ population is larger than IBG (left panel) and a second where the IBG population is larger than HREJ (right panel).

With these regions defined, the 3C50 model finds the IBG and HREJ populations of a target observation and compares them to a library of background spectra. This produces a scaled estimation of the background for a given GTI. We use the `nibackgen3C50 v5` tool to generate the 3C50 model for our entire set blank sky observations. We find that

<sup>7</sup>The 12.0–15.0 keV region was originally known as the high-energy background (HBG), giving this energy range the name IBG (Loewenstein, 2020).

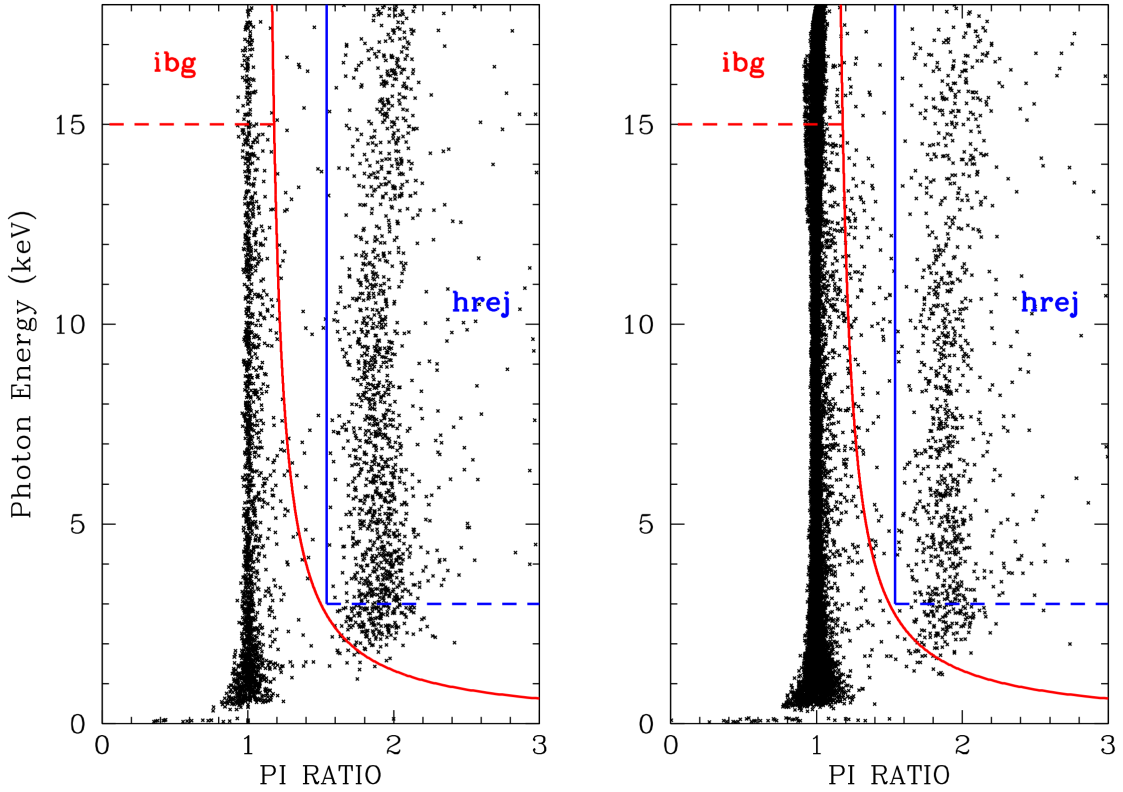


Figure 9: Comparison of HREJ and IBG populations for different *NICER* observations from Remillard (2019). On the left, the HREJ population contains more events, while the IBG contains more events in the right panel. The 3C50 model uses a library of spectral shapes for a grid of HREJ and IBG parameters.

the model is qualitatively consistent with the background spectra shown in Figure 7 at energies  $> 0.5$  keV, although it slightly overestimates the background. At softer energies, the model falls in between the dark Earth spectra and the four bright Earth angle ranges. We show a comparison of the 3C50 background model with these spectra in Figure 10.

#### 4.2 Environmental Background Model

The environmental background model takes an alternate approach to generate a background spectrum. Like the 3C50 model, the environmental model uses a library of background spectra that can be re-scaled based on the observational parameters. There are three environmental parameters used to describe the background in this model: cutoff rigidity (COR\_SAX), planetary geomagnetic index ( $K_p$ ), and Sun angle. The cutoff rigidity describes how the trajectory of particles resists bending when passing through a magnetic field (Pinilla et al., 2015). By definition, the cutoff rigidity is  $R = \frac{pc}{q}$ , where  $p$  is the momentum and  $q$  is the charge of the particle. The cutoff rigidity is an excellent indicator of Solar and cosmic rays, which constitute many of the background photons detected by *NICER*. While many Solar cosmic

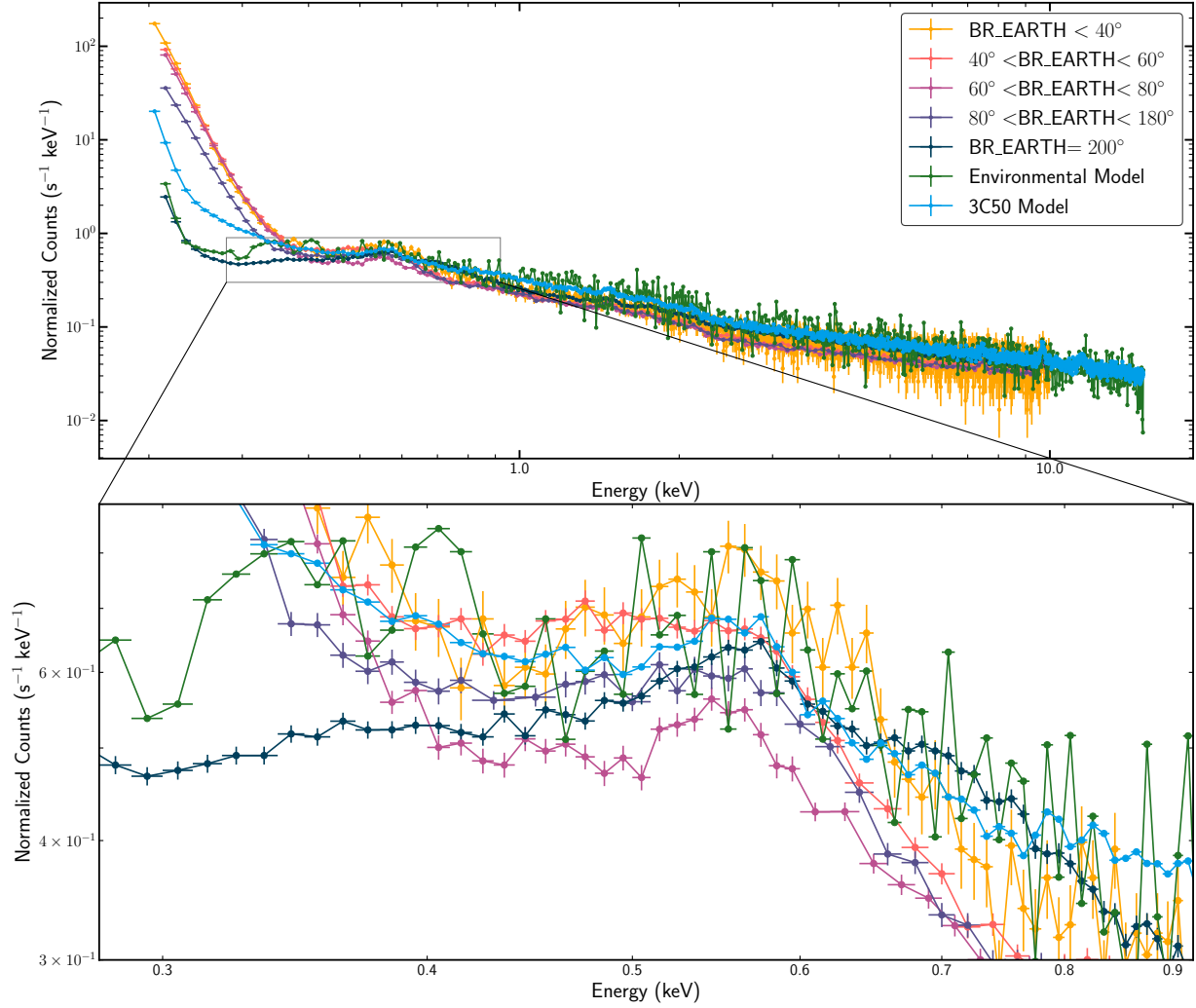


Figure 10: Comparison of bright Earth spectra from Figure 7 to 3C50 and environmental models. While the models are generally consistent at energies  $> 1.0$  keV, they diverge at soft X-ray energies.

rays are deflected by Earth's magnetosphere, high energy particles pass through and can interact with the detector (Kress et al., 2015).

The geomagnetic activity index, first defined by Bartels et al. (1939), describes disturbances in the Earth's magnetic field in three-hour windows on a 0–9 scale. The index is measured with a magnetometer at multiple sites around the Earth. A weighted average then produces the planetary geomagnetic index for the time window. On the 0–9 scale,  $K_p > 5$  indicates a geomagnetic storm. Even after events with high  $K_p$  are filtered out in standard processing, the index remains a useful diagnostic for modeling the time dependence of the environmental background.<sup>8</sup>

Finally, the Sun angle describes the pointing offset between the target and the vector from the Earth to the Sun. Again, even though this parameter is used as a part of the filtering process, typically requiring  $> 60^\circ$  separation, it is

<sup>8</sup>[https://heasarc.gsfc.nasa.gov/docs/nicer/science\\_nuggets/20180809.html](https://heasarc.gsfc.nasa.gov/docs/nicer/science_nuggets/20180809.html)

a useful metric for monitoring the loading of lower energy Solar particles on the detector. By combining these three metrics, the environmental model estimates the conditions of the particle environment during a given observation.

We generate an environmental background model for our set of blank sky observations using the Python implementation `nicer_bkg_estimator` v0.4. This takes the GTI's and filter file of an input spectra and uses a library of background spectra to create a scaled background. We show the generated environmental background in Figure 10 in green. We see that the environmental model has a larger scatter, especially at high energies. This is to be expected, especially in comparison to the 3C50 model. Whereas the 3C50 model is using the original, prefiltered data to estimate the background, the environmental model works with the cleaned GTIs. This means that we have more counts in the 3C50 model, and thus lower Poisson errors. In the 500–700 eV regime, the high scatter of the background model limits detailed comparisons. At the lowest energy regimes, the model is most consistent with the dark Earth observations (bright Earth angle  $200^\circ$ ). This suggests that the bright Earth angle could be incorporated as an additional scaling parameter to improve the accuracy of the model at the softest X-ray energies.

## 5 The Effects of Sun Angle

So far our investigation has suggested the relevance of the bright Earth angle in modeling the soft X-ray background. We perform an additional analysis to assess how the Sun angle affects our background spectra for each bright Earth range. Unlike the distribution of bright Earth angles, shown in Figure 6, the Sun angle distribution is not single peaked. Figure 11 shows the distribution of Sun angles for each bright Earth angle spectra. We divide each bright Earth angle into two spectra, with one corresponding to Sun angles below the median value and the other with Sun angles above the median value. This ensures we have equal counts in both spectra.

We repeat the spectra extraction procedure described in Section §3. Figure 12 show the ten Sun angle spectra corresponding to the five bright Earth angle ranges. We see that there are common energy regimes where the spectra diverge:  $< 500$  eV and 500–700 eV.

The variation in background spectra with respect to Sun angle, observed in all five bright Earth angle bands, confirms a dependence on Sun angle. This parameter is already used in the environmental model, and is expected to be correlated with the soft X-ray background because of optical loading and Solar energetic particles. We see that the scale of the variation, represented as the shaded gray area, varies noticeably with bright Earth angle. Below 500 eV, the difference between the two Sun angle spectra is substantial. However, for illuminated Earth observations with high Sun angle, the soft X-ray excess still exceeds that of the dark Earth spectra. This supports the reasoning that the bright Earth angle is a relevant parameter for considering the background at low energies.

The picture becomes more confusing for the 500–700 eV range. We see that the two Sun angle spectra cross over, and the shaded area is highly dependent on bright Earth angle. In the bright Earth angle range  $60^\circ < \text{BR\_EARTH} < 80^\circ$  the two Sun angle spectra show minimal difference in the 500–700 eV range, which is not the case for the neighboring bright Earth angle ranges. Furthermore, taking the  $40^\circ < \text{BR\_EARTH} < 60^\circ$  spectra as an example, we might have

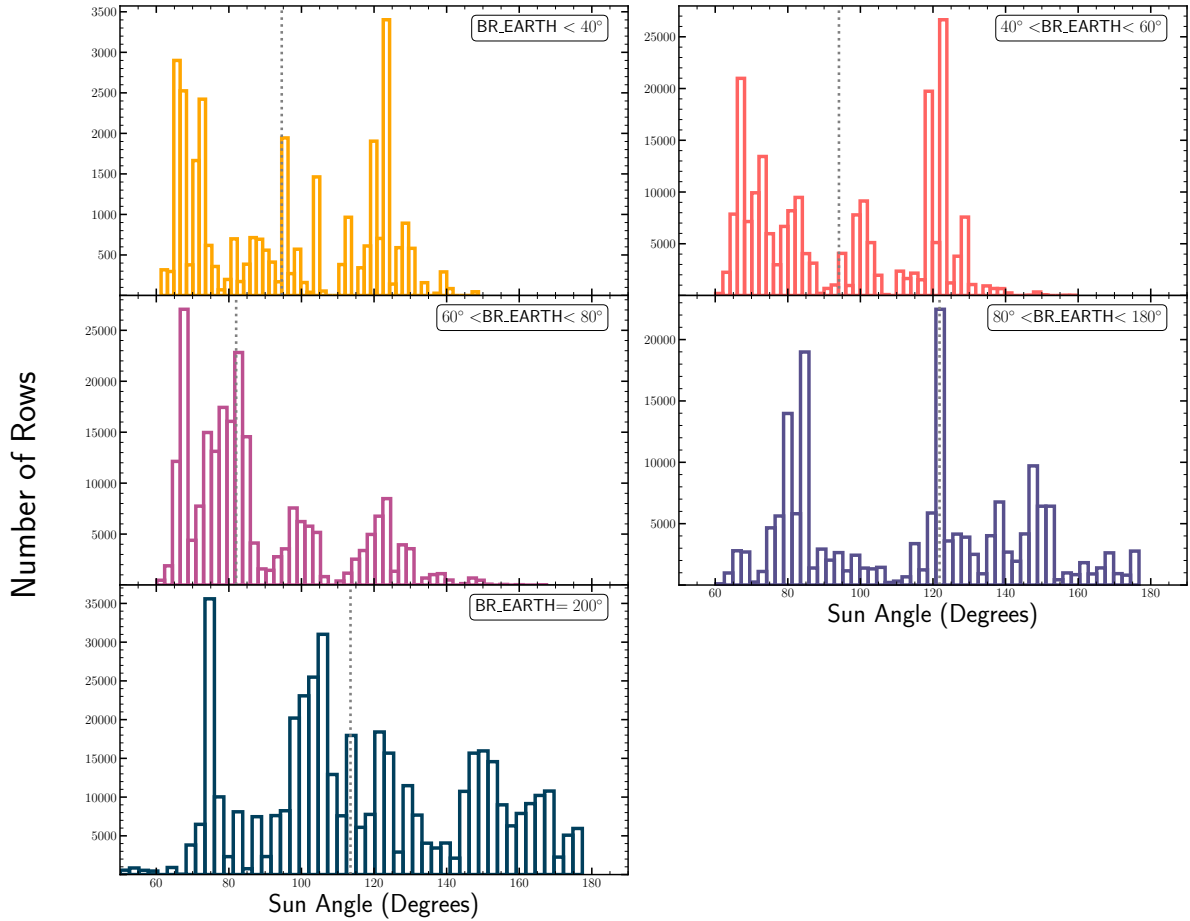


Figure 11: Distribution of Sun angle parameter for our five bright Earth angle spectra. The bright Earth angle range is labeled in the upper right of each panel. We find that the distribution is not single peaked and varies for each bright Earth range. The vertical gray line shows the median value.

expected the low Sun angle spectra to have higher excess at 500–700 eV. While this investigation is unable to provide a clear explanation for the observed spectral behavior, we have identified both the bright Earth angle and Sun angle as relevant parameters for future background modeling improvements.

## 6 Discussion and Conclusions

We have presented two years of *NICER* observations of seven blank sky regions. We have shown that the soft X-ray background emission is dependent on the bright Earth angle – the angle between the target pointing and the illuminated Earth limb. By comparing our observations with the two background models in circulation, we have demonstrated how they differ in their estimations of the soft X-ray background. We find that the environmental model agrees best with the dark Earth spectra. This suggests that the bright Earth angle should be included in the estimation routine, perhaps in a similar manner as the Sun angle parameter. The 3C50 model estimates the soft X-ray background  $< 500$  eV to

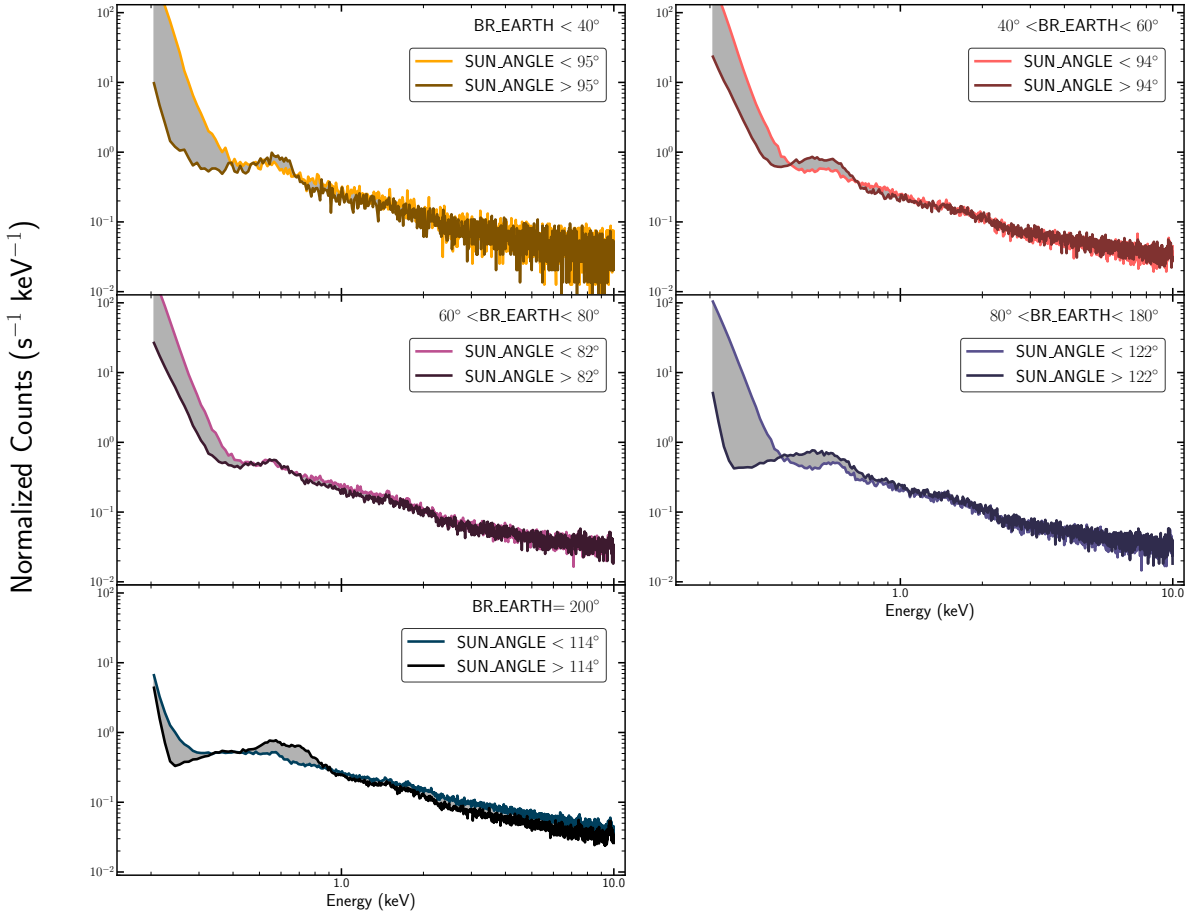


Figure 12: Comparison of the two Sun angle spectra for each bright Earth angle range. The bright Earth angle range is labeled in the upper right of each panel. We use the median value of the Sun angle to define the range for extraction. We shade the area in between each spectra in gray to improve clarity when comparing bright Earth ranges.

be in between the bright Earth and dark Earth spectra. A further investigation into the HREJ and IBG populations for different bright Earth angles may offer directions for how this model can be improved.

An additional analysis of Sun angle dependence yielded unexpected results. We found that the discrepancies between Sun angle selections varied with respect to bright Earth angle range. We identify two regions,  $< 500$  eV and  $500\text{--}700$  eV of particular interest. In the former, low Sun angles result in more observed background emission. In the  $500\text{--}700$  eV, range, where we expect to find line features from excited oxygen, we see that small angular separations result in more emission. While we cannot provide a clear interpretation of the results, they do suggest that both the bright Earth and Sun angles are relevant for estimations of the *NICER* soft X-ray background.

More generally, our results suggest that an accurate estimation of the *NICER* background requires careful consideration of a multitude of observational parameters. For the majority of *NICER* observations, a background model is required for spectral analysis. We therefore suggest a few directions to identify relevant dependencies of the soft X-ray background.

We found that spectra from low bright Earth angles differs significantly from dark Earth spectra. Approximately 40% of our observations were taken during dark Earth, but we do not distinguish between Earth angles in this category. A future study could seek to extend this analysis to Earth elevation angles of the dark Earth. This would allow for a more detailed comparison of dark and illuminated Earth observations.

It is clear that the specific observation geometry is extremely relevant for the observed X-ray background. An investigation into orbital position to compare observations taken in different regions of the Earth magnetosphere ([Fujimoto et al., 2007](#), Figure 8) could identify soft X-ray background dependencies.

Studies of the Solar wind charge exchange with *ROSAT* and *Suzaku* ([Snowden et al., 1994](#); [Fujimoto et al., 2007](#)) have identified temporal variations in the soft X-ray background, known as long term enhancements. A temporal investigation of the X-ray background may yield insights into what observational conditions are most relevant for the observed background. Comparisons with Solar activity data, such as Solar wind speed ([Smith et al., 2003](#)) or proton flux ([Snowden et al., 2004](#); [Fujimoto et al., 2007](#)) have revealed correlations in X-ray background observations from other telescopes. Cosmic ray occurrence rate is also known to vary with Solar cycle ([Smith et al., 2003](#)), which should be observed in the out-of-focus *NICER* observations. We briefly explore a temporal analysis of the background observations in Appendix A and discuss the feasibility of an extended study.

While it is unlikely that any single investigation will yield a ‘catch-all’ parameter for modeling the *NICER* X-ray background, by approaching this problem from different angles we will be able to unravel the various dependencies on observational parameters. Improving our understanding of the soft X-ray background is crucial for advancing the already deep scientific potential of *NICER*.

## 7 Acknowledgements

I would like to graciously thank Andrea Lommen for her guidance and advisement on this work. This project was developed in collaboration with Zaven Arzoumanian and Craig Markwardt, and I thank them for welcoming me into the *NICER* instrument team. I would also like to thank Mike Corcoran and Mike Loewenstein for their help in generating the background models. This work would not have been possible without the help of Joe Cammisa for managing the frequent software updates of HEAsoft. Finally, I would like to recognize the *NICER* Timing Working Group for offering regular feedback on this work.

## Appendix A Temporal Analysis of the Soft X-ray Background

In this work we have explored the spectral variation in the *NICER* soft X-ray background. Since the local particle environment is time dependent, we report initial investigations into the time-domain behavior of the observations presented in this study. During the study of *ROSAT* instrument calibration, [Snowden et al. \(1994\)](#) reported the detection

of ‘long term enhancements’ (LTEs) – periods where the X-ray background doubled in the lowest energy bands for timescales on the order of days.

Follow up studies suggested these LTEs were related to Solar wind charge exchange (Cox, 1998; Cravens, 2000) and found correlation between *ROSAT* LTEs and Solar wind proton-flux. Fujimoto et al. (2007) reported the detection of a long term enhancement in *Suzaku* observations of the north ecliptic pole. Spectral analysis of the flaring component showed a soft X-ray excess in emission lines and the addition of a power law component.

The *NICER* observations presented here vary in cadence (ranging from once a day to once every 10 days) and exposure. Figure 13 shows the total exposure of our observations after filtering as a function of time. While the exposure rate is roughly constant, we see a large increase at the end of 2017 and beginning of 2018. We therefore use the count rate, rather than counts, to investigate temporal variation. Figure 14 shows the count rate for our background observations. We see that while the count rate is typically  $\sim 1.25$  photons per second, there are several periods of enhanced X-ray emission in our observations.

We use data from the Solar Wind Electron Proton Alpha Monitor (SWEPAM) on the Advanced Composition Explorer (ACE, McComas et al., 1998) to find variations in the Solar wind during the *NICER* observing period. Figure 15 shows the proton speed and density from 2017 to May of 2019. We see that both the proton speed and density are highly variable. If the soft X-ray emission features observed in the *NICER* background are due to Solar wind charge exchange, we might find correlations through a temporal analysis.

A rigorous study of the temporal variations in the *NICER* X-ray background requires careful consideration of the filtering parameters. In fact, it may be interesting to consider how the filtering expressions given in Section §2 affect the light curve in Figure 14. For example, if the cutoff rigidity is effective in filtering cosmic ray detections, we should see variability coinciding with the Solar cycle if this filtering expression is removed. Correlation studies between *NICER* and Solar probes, like ACE or the Parker Solar Probe, offer direct comparisons with Solar activity statistics. These metrics could serve as a valuable addition to the environmental model.

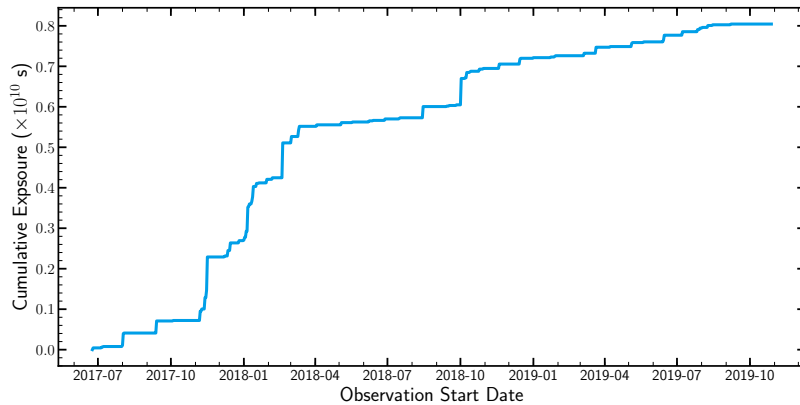


Figure 13: Cumulative exposure of the *NICER* background observations. We see that the observation cadence and duration results in a large increase in exposure at the end of 2017 through early 2018.

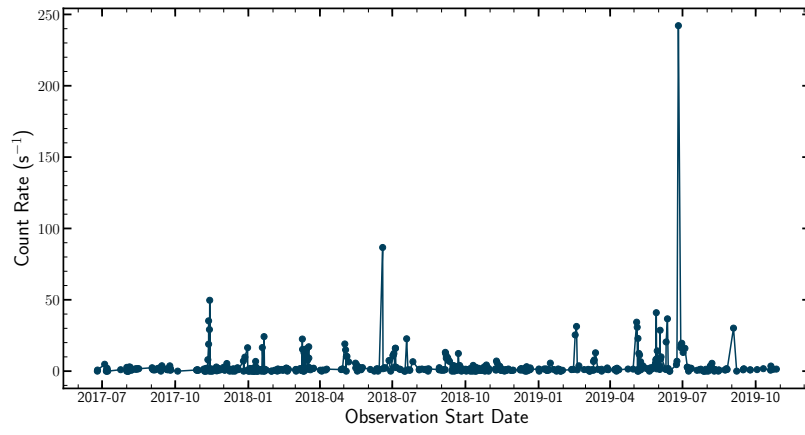


Figure 14: Count rate for the *NICER* background observations. We group observations by start date. While most observations have count rates of  $\sim 1.25 s^{-1}$ , we see non-periodic spikes in the count rate. These may be a potential point of investigation into the *NICER* X-ray background.

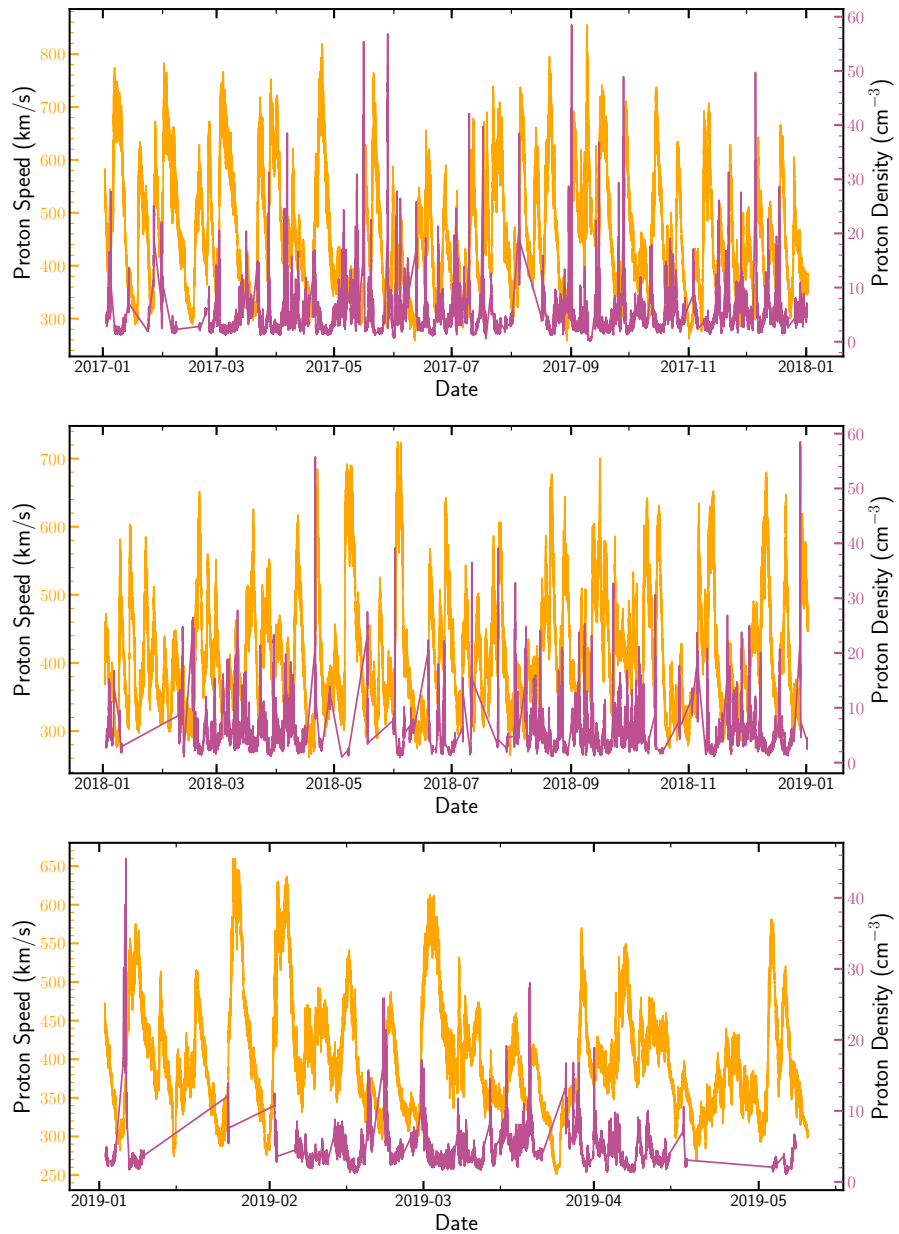


Figure 15: Solar wind proton speed and proton density from the SWEPAM on ACE. Data is only available through May of 2019. Both the proton speed and density vary in time, and may introduce temporal variation into the X-ray background.

## References

- Allen, S. W., Rapetti, D. A., Schmidt, R. W., et al. 2008, , 383, 879, doi: [10.1111/j.1365-2966.2007.12610.x](https://doi.org/10.1111/j.1365-2966.2007.12610.x)
- Arnaud, K., Dorman, B., & Gordon, C. 1999, XSPEC: An X-ray spectral fitting package. <http://ascl.net/9910.005>
- Arnaud, K. A. 1996, in Astronomical Society of the Pacific Conference Series, Vol. 101, Astronomical Data Analysis Software and Systems V, ed. G. H. Jacoby & J. Barnes, 17
- Arons, J. 1983, , 266, 215, doi: [10.1086/160771](https://doi.org/10.1086/160771)
- Arzoumanian, Z., Gendreau, K., Strohmayer, T., et al. 2019, The Astronomer's Telegram, 13239, 1
- Bartalucci, I., Mazzotta, P., Bourdin, H., & Vikhlinin, A. 2014, , 566, A25, doi: [10.1051/0004-6361/201423443](https://doi.org/10.1051/0004-6361/201423443)
- Bartels, J., Heck, N. H., & Johnston, H. F. 1939, Terrestrial Magnetism and Atmospheric Electricity (Journal of Geophysical Research), 44, 411, doi: [10.1029/TE044i004p00411](https://doi.org/10.1029/TE044i004p00411)
- Bilous, A. V., Watts, A. L., Harding, A. K., et al. 2019, , 887, L23, doi: [10.3847/2041-8213/ab53e7](https://doi.org/10.3847/2041-8213/ab53e7)
- Blandford, R., Meier, D., & Readhead, A. 2019, , 57, 467, doi: [10.1146/annurev-astro-081817-051948](https://doi.org/10.1146/annurev-astro-081817-051948)
- Bleeker, J. A. M., Burger, J. J., Deerenberg, A. J. M., et al. 1967, , 147, 391, doi: [10.1086/149019](https://doi.org/10.1086/149019)
- Boella, G., Butler, R. C., Perola, G. C., et al. 1997, , 122, 299, doi: [10.1051/aas:1997136](https://doi.org/10.1051/aas:1997136)
- Bowyer, S., Byram, E. T., Chubb, T. A., & Friedman, H. 1964, Science, 146, 912, doi: [10.1126/science.146.3646.912](https://doi.org/10.1126/science.146.3646.912)
- Carter, J. A., & Sembay, S. 2009, in American Institute of Physics Conference Series, Vol. 1156, American Institute of Physics Conference Series, ed. R. K. Smith, S. L. Snowden, & K. D. Kuntz, 100–104
- Cerutti, B., Philippov, A. A., & Spitkovsky, A. 2016, , 457, 2401, doi: [10.1093/mnras/stw124](https://doi.org/10.1093/mnras/stw124)
- Cheng, K. S., Ho, C., & Ruderman, M. 1986, , 300, 500
- Cox, D. P. 1998, Modeling the Local Bubble, ed. D. Breitschwerdt, M. J. Freyberg, & J. Truemper, Vol. 506, 121–131
- Cravens, T. E. 2000, , 532, L153, doi: [10.1086/312574](https://doi.org/10.1086/312574)
- Cravens, T. E., Robertson, I. P., Snowden, S., et al. 2009, in American Institute of Physics Conference Series, Vol. 1156, American Institute of Physics Conference Series, ed. R. K. Smith, S. L. Snowden, & K. D. Kuntz, 37–51
- Deneva, J. S., Ray, P. S., Lommen, A., et al. 2019, arXiv e-prints, arXiv:1902.07130. <https://arxiv.org/abs/1902.07130>
- Dubner, G., Castelletti, G., Kargaltsev, O., et al. 2017, , 840, 82, doi: [10.3847/1538-4357/aa6983](https://doi.org/10.3847/1538-4357/aa6983)
- Dyks, J., & Rudak, B. 2003, , 598, 1201, doi: [10.1086/379052](https://doi.org/10.1086/379052)
- Forman, W., Jones, C., Cominsky, L., et al. 1978, , 38, 357, doi: [10.1086/190561](https://doi.org/10.1086/190561)
- Fraser, G. W. 1989, X-ray detectors in astronomy
- Fujimoto, R., Mitsuda, K., Mccammon, D., et al. 2007, , 59, 133, doi: [10.1093/pasj/59.sp1.S133](https://doi.org/10.1093/pasj/59.sp1.S133)
- Gendreau, K. 2019, personal communication
- Gendreau, K., & Arzoumanian, Z. 2017, Nature Astronomy, 1, 895, doi: [10.1038/s41550-017-0301-3](https://doi.org/10.1038/s41550-017-0301-3)
- Giacconi, R., Gursky, H., Paolini, F. R., & Rossi, B. B. 1962, , 9, 439, doi: [10.1103/PhysRevLett.9.439](https://doi.org/10.1103/PhysRevLett.9.439)
- Giacconi, R., Rosati, P., Tozzi, P., et al. 2001, , 551, 624, doi: [10.1086/320222](https://doi.org/10.1086/320222)
- Glendenning, N. K. 1985, , 293, 470, doi: [10.1086/163253](https://doi.org/10.1086/163253)
- Gomez, H. L., Krause, O., Barlow, M. J., et al. 2012, , 760, 96, doi: [10.1088/0004-637X/760/1/96](https://doi.org/10.1088/0004-637X/760/1/96)
- Güver, T., Göğüş, E., Vurgun, E., et al. 2019, , 877, L30, doi: [10.3847/2041-8213/ab212d](https://doi.org/10.3847/2041-8213/ab212d)
- Haardt, F., & Maraschi, L. 1991, , 380, L51, doi: [10.1086/186171](https://doi.org/10.1086/186171)
- Hwang, U., & Laming, J. M. 2012, , 746, 130, doi: [10.1088/0004-637X/746/2/130](https://doi.org/10.1088/0004-637X/746/2/130)
- Jahoda, K., Markwardt, C. B., Radeva, Y., et al. 2006, , 163, 401, doi: [10.1086/500659](https://doi.org/10.1086/500659)
- Jansen, F., Lumb, D., Altieri, B., et al. 2001, , 365, L1, doi: [10.1051/0004-6361:20000036](https://doi.org/10.1051/0004-6361:20000036)
- Kalapotharakos, C., Harding, A. K., & Kazanas, D. 2014, , 793, 97, doi: [10.1088/0004-637X/793/2/97](https://doi.org/10.1088/0004-637X/793/2/97)
- Kara, E., Pasham, D., Gendreau, K., & Arzoumanian, Z. 2019, The Astronomer's Telegram, 13132, 1

- Koutroumpa, D., Lallement, R., & Kharchenko, V. 2009, in American Institute of Physics Conference Series, Vol. 1156, American Institute of Physics Conference Series, ed. R. K. Smith, S. L. Snowden, & K. D. Kuntz, 62–73
- Kress, B. T., Hudson, M. K., Selesnick, R. S., Mertens, C. J., & Engel, M. 2015, Journal of Geophysical Research: Space Physics, 120, 5694, doi: [10.1002/2014JA020899](https://doi.org/10.1002/2014JA020899)
- Kuntz, K. D., & Snowden, S. L. 2000, , 543, 195, doi: [10.1086/317071](https://doi.org/10.1086/317071)  
—. 2008, , 478, 575, doi: [10.1051/0004-6361:20077912](https://doi.org/10.1051/0004-6361:20077912)
- Lattimer, J. M., & Prakash, M. 2007, , 442, 109, doi: [10.1016/j.physrep.2007.02.003](https://doi.org/10.1016/j.physrep.2007.02.003)
- Lee, H., Kashyap, V. L., van Dyk, D. A., et al. 2011, , 731, 126, doi: [10.1088/0004-637X/731/2/126](https://doi.org/10.1088/0004-637X/731/2/126)
- Lewin, W., & van der Klis, M. 2010, Compact Stellar X-ray Sources
- Loewenstein, M. 2020, personal communication
- Ludlam, R. M., Miller, J. M., Arzoumanian, Z., et al. 2018, , 858, L5, doi: [10.3847/2041-8213/aabee6](https://doi.org/10.3847/2041-8213/aabee6)
- Lumb, D. H., Schartel, N., & Jansen, F. A. 2012, Optical Engineering, 51, 011009, doi: [10.1117/1.OE.51.1.011009](https://doi.org/10.1117/1.OE.51.1.011009)
- Lumb, D. H., Warwick, R. S., Page, M., & De Luca, A. 2002, , 389, 93, doi: [10.1051/0004-6361:20020531](https://doi.org/10.1051/0004-6361:20020531)
- McComas, D. J., Bame, S. J., Barker, P., et al. 1998, , 86, 563, doi: [10.1023/A:1005040232597](https://doi.org/10.1023/A:1005040232597)
- Miller, J. M., Bautz, M. W., & McNamara, B. R. 2017, , 850, L3, doi: [10.3847/2041-8213/aa9566](https://doi.org/10.3847/2041-8213/aa9566)
- Miller, J. M., Kammoun, E., Ludlam, R. M., et al. 2019a, , 884, 106, doi: [10.3847/1538-4357/ab3e05](https://doi.org/10.3847/1538-4357/ab3e05)
- Miller, M. C., Lamb, F. K., Dittmann, A. J., et al. 2019b, , 887, L24, doi: [10.3847/2041-8213/ab50c5](https://doi.org/10.3847/2041-8213/ab50c5)
- Morello, V., Keane, E. F., Enoto, T., et al. 2019, arXiv e-prints, arXiv:1910.04124. <https://arxiv.org/abs/1910.04124>
- Murdin, P., ed. 2000, Uhuru (SAS-1/Explorer 42), 4774
- Muslimov, A. G., & Harding, A. K. 2003, , 588, 430, doi: [10.1086/368162](https://doi.org/10.1086/368162)
- Ng, C. Y., Takata, J., Leung, G. C. K., Cheng, K. S., & Philippopoulos, P. 2014, , 787, 167, doi: [10.1088/0004-637X/787/2/167](https://doi.org/10.1088/0004-637X/787/2/167)
- Nice, D. J. 2006, Advances in Space Research, 38, 2721, doi: [10.1016/j.asr.2006.04.024](https://doi.org/10.1016/j.asr.2006.04.024)
- Okajima, T., Soong, Y., Balsamo, E. R., et al. 2016, in Society of Photo-Optical Instrumentation Engineers (SPIE) Conference Series, Vol. 9905, Space Telescopes and Instrumentation 2016: Ultraviolet to Gamma Ray, 99054X
- Pinilla, S., Asorey, H., & Núñez, L. A. 2015, Nuclear and Particle Physics Proceedings, 267-269, 418, doi: [10.1016/j.nuclphysbps.2015.10.139](https://doi.org/10.1016/j.nuclphysbps.2015.10.139)
- Prigozhin, G., Gendreau, K., Doty, J. P., et al. 2016, in Society of Photo-Optical Instrumentation Engineers (SPIE) Conference Series, Vol. 9905, Space Telescopes and Instrumentation 2016: Ultraviolet to Gamma Ray, 99051I
- Raijmakers, G., Riley, T. E., Watts, A. L., et al. 2019, , 887, L22, doi: [10.3847/2041-8213/ab451a](https://doi.org/10.3847/2041-8213/ab451a)
- Ray, P. S., Guillot, S., Ho, W. C. G., et al. 2019a, , 879, 130, doi: [10.3847/1538-4357/ab24d8](https://doi.org/10.3847/1538-4357/ab24d8)
- Ray, P. S., Guillot, S., Ransom, S. M., et al. 2019b, , 878, L22, doi: [10.3847/2041-8213/ab2539](https://doi.org/10.3847/2041-8213/ab2539)
- Remillard, R. 2019, personal communication
- Riley, T. E., Watts, A. L., Bogdanov, S., et al. 2019, , 887, L21, doi: [10.3847/2041-8213/ab481c](https://doi.org/10.3847/2041-8213/ab481c)
- Risaliti, G., Harrison, F. A., Madsen, K. K., et al. 2013, , 494, 449, doi: [10.1038/nature11938](https://doi.org/10.1038/nature11938)
- Rodney, S. A., & Tonry, J. L. 2006, , 118, 866, doi: [10.1086/505089](https://doi.org/10.1086/505089)
- Rowan, D. M., Ghazi, Z., Lugo, L., et al. 2020, arXiv e-prints, arXiv:2001.11513. <https://arxiv.org/abs/2001.11513>
- Smith, E. J., Marsden, R. G., Balogh, A., et al. 2003, Science, 302, 1165, doi: [10.1126/science.1086295](https://doi.org/10.1126/science.1086295)
- Snowden, S. L., Collier, M. R., & Kuntz, K. D. 2004, , 610, 1182, doi: [10.1086/421841](https://doi.org/10.1086/421841)
- Snowden, S. L., McCammon, D., Burrows, D. N., & Mendenhall, J. A. 1994, , 424, 714, doi: [10.1086/173925](https://doi.org/10.1086/173925)
- Snowden, S. L., Freyberg, M. J., Plucinsky, P. P., et al. 1995, , 454, 643, doi: [10.1086/176517](https://doi.org/10.1086/176517)
- Strüder, L., Briel, U., Dennerl, K., et al. 2001, , 365, L18, doi: [10.1051/0004-6361:20000066](https://doi.org/10.1051/0004-6361:20000066)
- Strüder, L. 2000, Nuclear Instruments and Methods in Physics Research Section A: Accelerators, Spectrometers, Detectors and Associated Equipment, 454, 73 , doi: [https://doi.org/10.1016/S0168-9002\(00\)00811-1](https://doi.org/10.1016/S0168-9002(00)00811-1)

- Temim, T., Gehrz, R. D., Woodward, C. E., et al. 2006, , 132, 1610, doi: [10.1086/507076](https://doi.org/10.1086/507076)
- Thorsett, S. E., & Chakrabarty, D. 1999, , 512, 288, doi: [10.1086/306742](https://doi.org/10.1086/306742)
- Turner, M. J. L., Abbey, A., Arnaud, M., et al. 2001, , 365, L27, doi: [10.1051/0004-6361:20000087](https://doi.org/10.1051/0004-6361:20000087)
- Verbunt, F., Kuiper, L., Belloni, T., et al. 1996, , 311, L9
- Wang, J., Kara, E., Steiner, J., et al. 2019, arXiv e-prints, arXiv:1910.01245. <https://arxiv.org/abs/1910.01245>
- Weisskopf, M. C., Tananbaum, H. D., Van Speybroeck, L. P., & O'Dell, S. L. 2000, Society of Photo-Optical Instrumentation Engineers (SPIE) Conference Series, Vol. 4012, Chandra X-ray Observatory (CXO): overview, ed. J. E. Truemper & B. Aschenbach, 2–16
- Wikipedia contributors. 2020, List of X-ray space telescopes — Wikipedia, The Free Encyclopedia. [https://en.wikipedia.org/w/index.php?title=List\\_of\\_X-ray\\_space\\_telescopes&oldid=942839422](https://en.wikipedia.org/w/index.php?title=List_of_X-ray_space_telescopes&oldid=942839422)